THE SPECTRAL RADIATIVE EFFECT OF Si/SiO_2 SUBSTRATE ON MONOLAYER ALUMINUM POROUS MICROSTRUCTURE

by

Haiyan YU, Haochun ZHANG*, Chengshuai SU, Kexin WANG, and Liang JIN
School of Energy Science and Engineering, Harbin Institute of Technology, Harbin, China

Original scientific paper
https://doi.org/10.2298/TSCI171125047Y

In this work, we have investigated theoretically the spectral radiative properties of a monolayer aluminum porous microstructure, including wavelength-selective transmission, reflection, and absorption. The finite-difference time-domain method for electromagnetics has been used to calculate the spectral radiative properties of the monolayer aluminum porous microstructure. It is found that the absorption spectra of the aluminum porous microstructure will generate two peaks within the wavelength ranging from 1.0 to 15.0 μm at normal incidence of light. Then the surface plasma polarition resonance could be observed clearly in the obtained results of this work, especially on the top surface near the orifice. Inside the porous structure, magnetic polariton is the crucial mechanism to elucidate for the power absorption enhancement. Furthermore, the absorption capacity of the aluminum porous structure with Si/SiO_2 substrate has been analyzed, to explain the influence of base on the monolayer porous material. The findings indicate that the absorptance peak at 3 μm incident wavelength significantly improved with silicon substrate, while that of silica substrate has little difference with aluminum porous plate. The silicon and silica bases disrupted the distribution of the electromagnetic fields of the original aluminum porous structure, and form a new magnetic field within the subbases. Meanwhile the internal microcavity polarition of the porous structure has enhanced obviously near the bases.

Key words: *porous microstructure, radiative, absorptance, substrate*

Introduction

To achieve perfect radiative characteristics of micro nanostructure in different wavelength ranges is of vital importance in applications such as solar energy harvesting [1], aircraft radiative cooling [2], and chemical sensing [3]. Thorough development of the fundamentals of microscale radiation is available in recent research, such as surface plasmon polaritons [4, 5], microcavity resonance effect [6, 7], and photon tunneling effect [8, 9], *etc*. In the early 1970s, microscale radiation effect was found by Zang and Tien *et al*. [10, 11]. Then simulation receives more recognition with the rapid expanding of computer technology in microscale radiation. Mulet *et al*. [12] and Francoeur *et al*. [13] pointed out that the magnitude of microscale radiation heat transfer between two closely semi-infinite plates exceeded Planck's blackbody radiation. Liu *et al*. [14] studied near-field radiative heat transfer of Si based metamaterials using fluctuation electrodynamics method. The general method to deal with microscale heat transfer prob-

*Corresponding author, e-mail: ces@vip.126.com

lems was based on fluctuation dissipation theorem [15]. The other general method to solve microscale radiative without heat transfer is based on discrete Maxwell equations combined with material equations [16]. Fu *et al*. [17] simulated reflectance of 1-D random roughness surface by using finite-difference time-domain (FDTD). Chen *et al*. [18] numerically investigated optical responses of deep slits at transverse magnetic by using rigorous coupled-wave analysis and found that the optical response was much different for slits with different attached features. Klimov *et al*. [19] reported on the fundamental constraints pertaining to the enhancement of the radiative emission rate achievable with planar lamellar metamaterials of any kind. Zheng [20] focused on a methodology about adjusting the wavelength selectivity of thin films embedded with nanoparticles.

So far, current researches on the porous array microstructures mostly stay in the preparation stage, while the comprehensive studies of their spectral radiative properties are still demanded. In this study, we investigated theoretically the spectral radiative properties of a porous microstructure using the FDTD method for electromagnetics. Aluminum was chosen as the material for its ability of temperature stability and ease to electrochemical processing. The structure contained the arrays of uniformly sized spherical pores which ordered closely inside and the whole void spaces between the pores are filled up with aluminum. Moreover, the spectral radiative properties of the porous microstructure have been studied when the basis of different materials substrate added. Finally we explored the energy absorption distribution and how to enhance the mechanism of absorption of the aluminum porous microstructure.

Physical model

Aluminum metal foam can be fabricated by some mature methods such as the preparation methods of inverse opals. Among these methods, the colloidal crystal-templating approach has been used to prepare 3-D ordered porous materials [21]. The aluminum porous cell that was obtained by means of inverse opals method can be simplified into a spherical porous element cell model which was shown in fig. 1, with two following assumptions: there is no metal oxidation on the surface of aluminum and the element is a smooth surface. The porosity of each cell was 0.77, the height of aluminum porous monolayer, *l,* and the edge length of aluminum cell was 2.54 m and the radius of the inner porous, *r*, was 1.5 m. The Si and SiO_2 with their excellent spectral radiation controlling ability are commonly used in optical components especially as substrate material which was shown in fig. 2.

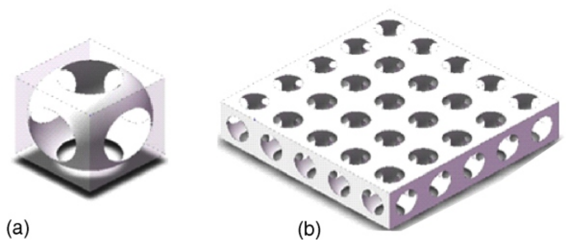

Figure 1. The microporous configuration; (a) porous cell (b) porous monolayer structure

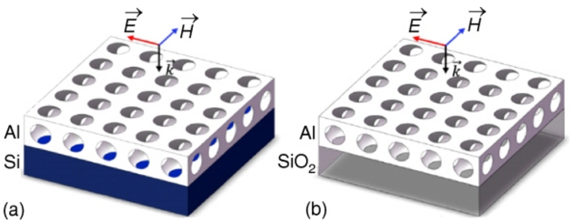

Figure 2. The microporous substrate models configuration; (a) Si substrate structure (b) SiO_2 substrate structure

In this paper, we use these models to study the effect of the substrate on the aluminum porous monolayer structure. To simplify the calculation, we assume that the substrate layer height, *h*, was in direct proportion to the height of aluminum porous monolayer, l, and the proportional coefficient was here a constant equal to $h/l = 1$.

Numerical details

Governing equations

The finite volume modeling was conducted by applying the simulation software FDTD. The basic theory of Maxwell function can govern the distribution of electromag-netic phenomena, whose curl equations and constitutive equations are written:

$$\boldsymbol{H} \quad \frac{\partial \boldsymbol{D}}{\partial t} \quad \boldsymbol{J} \tag{1a}$$

$$\boldsymbol{E} \quad \frac{\partial \boldsymbol{B}}{\partial t} \quad \boldsymbol{M} \tag{1b}$$

$$\boldsymbol{B} \quad \rho_{\mathrm{e}} \tag{1c}$$

$$\boldsymbol{D} \quad \rho_{\mathrm{m}} \tag{1d}$$

where H [V/m] is the magnetic field intensity, E [A/m] – the electric field intensity, B [Wb/m^2] – the magnetic flux density, D [C/m^2] – the electric displacement vector, J [A/m^2] – the current density, t [s] – the time, ρ [C/m^3] – the designed the volume charge density. The eqs. (1a) and (1b) describe, respectively, the interaction of electric field intensity and magnetic flux density in a vacuum. The material equations are given [20]:

$$\boldsymbol{D} \quad \varepsilon \boldsymbol{E} \tag{2a}$$

$$\boldsymbol{B} \quad \mu \boldsymbol{H} \tag{2b}$$

$$\boldsymbol{J} \quad \sigma \boldsymbol{E} \tag{2c}$$

where ε [F/m] is the permittivity, μ [H/m] – the permeability, σ [S/m] – the conductivity. Finally, the Maxwell function is obtained by inserting eqs. (2) into eqs. (1) as eqs. (3):

$$\boldsymbol{H} \quad \varepsilon \frac{\partial \boldsymbol{E}}{\partial t} \quad \sigma \boldsymbol{E} \tag{3a}$$

$$\boldsymbol{E} \quad \mu \frac{\partial \boldsymbol{H}}{\partial t} \tag{3b}$$

$$\boldsymbol{H} \quad 0 \tag{3c}$$

$$\boldsymbol{E} \quad \frac{\rho}{\varepsilon} \tag{3d}$$

In 3-D Cartesian co-ordinate system, these equations can be written as eqs. (4):

$$\frac{\partial \boldsymbol{H}_x}{\partial t} \quad \frac{1}{\mu_x} \quad \frac{\partial \boldsymbol{E}_y}{\partial z} \quad \frac{\partial \boldsymbol{E}_z}{\partial y} \quad \sigma_x^m \boldsymbol{H}_x \tag{4a}$$

$$\frac{\partial \boldsymbol{H}_y}{\partial t} \quad \frac{1}{\mu_y} \quad \frac{\partial \boldsymbol{E}_z}{\partial z} \quad \frac{\partial \boldsymbol{E}_x}{\partial y} \quad \sigma_y^m \boldsymbol{H}_y \tag{4b}$$

$$\frac{\partial \boldsymbol{H}_z}{\partial t} \quad \frac{1}{\mu_z} \quad \frac{\partial \boldsymbol{E}_x}{\partial z} \quad \frac{\partial \boldsymbol{E}_y}{\partial y} \quad \sigma_z^m \boldsymbol{H}_z \tag{4c}$$

$$\frac{\partial \boldsymbol{E}_x}{\partial t} \quad \frac{1}{\varepsilon_x} \quad \frac{\partial \boldsymbol{H}_z}{\partial y} \quad \frac{\partial \boldsymbol{H}_y}{\partial z} \quad \sigma_x^e \boldsymbol{E}_x \tag{4d}$$

$$\frac{\partial \boldsymbol{E}_y}{\partial t} \quad \frac{1}{\varepsilon_y} \quad \frac{\partial \boldsymbol{H}_x}{\partial z} \quad \frac{\partial \boldsymbol{H}_z}{\partial x} \quad \sigma_y^e \boldsymbol{E}_y \tag{4e}$$

$$\frac{\partial \boldsymbol{E}_z}{\partial t} \quad \frac{1}{\varepsilon_z} \quad \frac{\partial \boldsymbol{H}_y}{\partial x} \quad \frac{\partial \boldsymbol{H}_x}{\partial y} \quad \sigma_z^e \boldsymbol{E}_z \tag{4f}$$

where x, y, and z are the axis in the Cartesian co-ordinate system. Equations (4) establishes the relationship between Maxwell function and physical model media. During the calculation, the top and bottom are treated as the perfectly matched boundary-layer conditions.

Absorption scattering cross-section

In electromagnetic theory, the absorption scattering cross-section is defined:

$$\langle \boldsymbol{S}^{(i)} \rangle \quad \frac{c}{8\pi} Re\{\boldsymbol{E}^{(i)} \quad \boldsymbol{H}^{(i)*}\} \tag{5}$$

$$W^{(a)} \quad \frac{c}{8\pi} Re \underset{\Sigma}{} [E^{(i)} \quad H^{(s)*} \quad E^{(s)} \quad (H^{(i)*} \quad H^{(s)*})] n \mathrm{d}x\mathrm{d}y \tag{6}$$

where S is the Poynting vector, n – the unit outward normal, $W^{(a)}$ [W/s] – the rate of absorption scattering, $\langle\,\rangle$ – the system average, superscript (i) – the incidence, (s) – the scattering, * – the conjugate complex vector, and Re – the real part. Ratio $W^{(a)}/S^{(i)}$ is:

$$Q^{(a)} \quad \frac{W^{(a)}}{|\langle S^{(i)} \rangle|} \quad \frac{Re \underset{\Sigma}{} [E^{(i)} \quad H^{(s)*} \quad E^{(s)} \quad (H^{(i)*} \quad H^{(s)*})] n \mathrm{d}x\mathrm{d}y}{Re(E^{(i)} \quad H^{(i)*})} \tag{7}$$

where $Q^{(a)}$ [m^2] is the absorption cross-section. When it comes to monolayer microstructure is composed its absorptive capacity can be expressed as the absorptive capacity:

$$A \quad 1 \quad \frac{(S^{(r)} \quad S^{(t)}) g n \mathrm{d}x\mathrm{d}y}{S^{(i)} g n \mathrm{d}x\mathrm{d}y} \tag{8}$$

where $S^{(r)}$ represents the energy of reflection, while $S^{(t)}$ is the transmission energy flow. The A is the absorptance. In the same way, reflectance R and transmittance T can be expressed as eqs. (9) and (10):

$$R \quad \frac{S^{(r)} g n \mathrm{d}x\mathrm{d}y}{S^{(i)} g n \mathrm{d}x\mathrm{d}y} \tag{9}$$

$$T \quad \frac{S^{(t)} g n \mathrm{d}x\mathrm{d}y}{S^{(i)} g n \mathrm{d}x\mathrm{d}y} \tag{10}$$

In this paper eqs. (9)-(11) were used to study the spectral radiant characteristics of high porosity aluminum porous monolayer structure with different bases.

Result and discussion

These computations were carried out on a 3.4 GHz Intel 8-Core E3-1231-v3 processor Windows 7 server and 16 GB RAM. The incidence was TEM wave ranging of 0.1 m λ 15 m, which was divided into 300 intervals for spectral calculations. In this study, a mesh size of $\lambda/100$ was used, depending the checking of the grid independence.

The previous dielectric constant was calculated by using the *n*, *k* model. The absorbance of the monolayer aluminum cell structure was available according to the Drude model [22]. The different Drude models were used to calculate the absorptance of the monolayer spherical porous aluminum structure as shown in fig. 3. The dielectric constant of the material was different when the Drude model was used to describe the change of the absorption curve. In the range of 1~3 m, there was an irregular absorption peak, which was relatively smaller compared to 4.3 m wavelength, and the peak at 4.3 μm does not change with the Drude model changing. It can also be found that the absorbance of the model was the same, and the absorption rate of the *n* and *k* models was the smallest. However, at 0.43 m, the absorption rate of the *n* and *k* models was 0.3, with the absorbance of the Drude model increasing to 0.6.

Figure 4 showed that in the infrared band range of 1~15 m, the infinite aluminum plate absorptance was 0. The electromagnetic waves are almost all reflected when vertical incidence. The aluminum plate showed full reflection characteristic in the middle and near infrared band. For the aluminum porous monolayer struc-

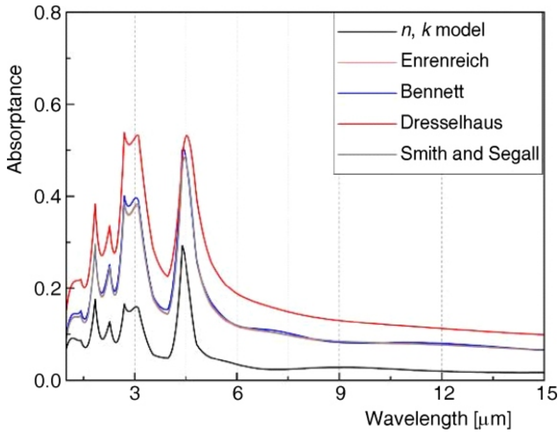

Figure 3. Absorbance of different drude models

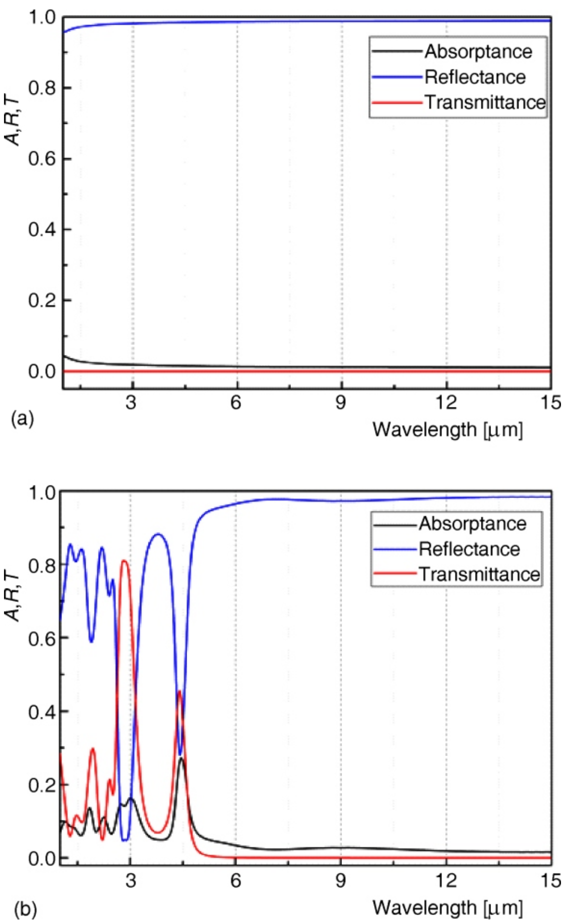

Figure 4. The spectral radiative properties; (a) aluminum plate (b) aluminum porous monolayer structure

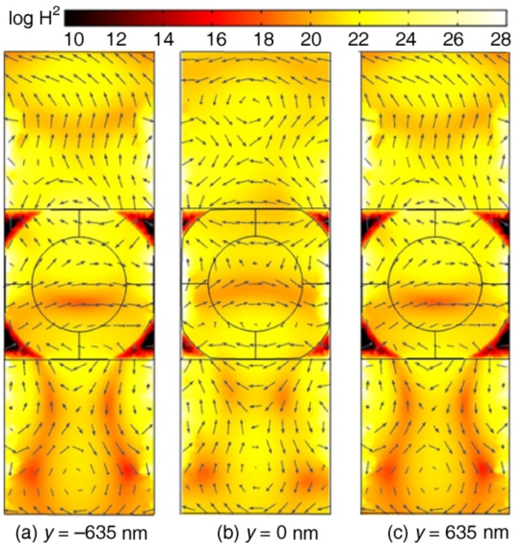

Figure 5. The current density distribution when the incidence wavelength is 2.86 μm

ture, keeping the incident conditions unchanged, its absorptance, transmission than the flat structure has undergone great changes. What is more, at 3 m wavelength, the value of absorptance can reach 0.28, while at 4.5 m wavelength, it was up to 0.3. In general, the surface plasma formation of the polarition was easy to produce irregular peaks, and a wide peak can be found easily in the magnetic polarition formation of the resonance. To illustrate this phenomenon more clearly, we drawn the electric field distribution and magnetic field intensity at these two places.

Figure 5 showed the current density distribution and schematic of the aluminum porous monolayer microstructure at normal incidence of wave-length λ = 2.86 m. There are three sections along y-axis, locating at, y = –635 nm, y = 0 nm, and y = 635 nm, respectively. The color contour shows the amplitude of the magnetic field, while the arrows denote the instantaneous the direction of the current density. It was obvious that there are two closed loops formed by the induced current near the upper and lower surfaces of porous structure. On the basis of Lenz's law, these two new magnetic fields are activated by the induced current along the direction of x-axis which was opposite to the direction of the incident magnetic field. It can be seen that this resonance exists only near surface area and attenuates rapidly, which was a typical characteristic of the surface plasma resonance (SPR).

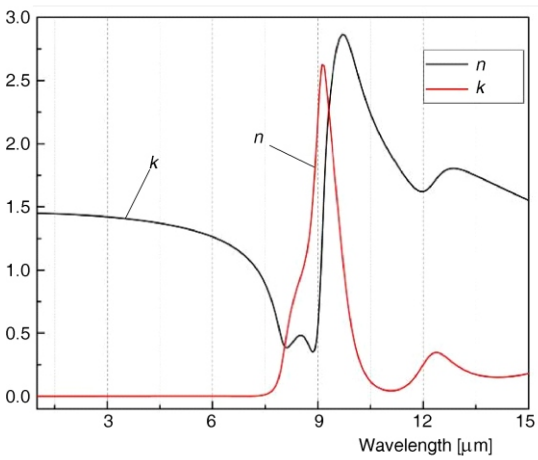

Figure 6. The SiO^2 refractive index with the wavelength of the relationship

In order to consider the influence of the base on the structure, the base of the aluminum was added to Si/SiO_2 substrate under the monolayer. In this research, the thickness of Si and SiO_2 substrates was 2.54 m. At the wavelength ranging from 1~15 m, Si is a non-dispersive material, whose refractive index is usually 3.4, comparing with SiO_2. The refractive index of the real and imaginary parts [22] with the wavelength of the relationship is shown in fig. 6.

The SiO_2 material is a dielectric, as well as a dispersion material in the infrared band. The real part reduced with the increase in wavelength of 1~ 6 m, while the imaginary part was kept at 0. When the wavelength ranging from 6.5~9 m, the real part also produced a sharper change, while the imaginary part raised a large protrusions and rapid declined. Using these characteristics of SiO$_2$ material, a control devices with radiation characteristics can be well designed. Based on the previous data, we obtained the Si substrate and SiO$_2$ substrate absorption transmission and reflection diagram as shown in fig. 7.

From fig. 7, the continuous irregular peaks are generated in the 1~6 m band. The peaks are sharper and the width is narrower, in this band, the resonant state was strong, and the curve was almost no change in the 6~15 m band. The trend was consistent with that of the flat plate, indicating that the change of the structure in the band will not affect the optical radiation characteristics of the material. The difference was that the transmittance and reflectance curves of the graph are sharper in the range of the wavelength from 1-5 m. The absorptance curve of the peak was not so sharp.

Figure 8 showed the relationship between the absorptance of the monolayer spherical porous aluminum structure, Si monolayer spherical porous aluminum structure, and SiO$_2$ monolayer spherical porous aluminum structure with wavelength. The absorption rates of three structures are fluctuating in the range of 1~6 m, while these three absorption curves coincide with each other, in the 6~15 m band. The trend was consistent with the aluminum plate on increasing and changing. The absorptance of Si substrate had little difference with that of porous aluminum plate. To further analyze the mechanism reason of absorption peaks, figs. 9 and 10 were mapped to describe the electric field and magnetic intensity in these two places.

Figure 9 showed the current density distribution and schematic of the aluminum porous monolayer microstructure and Si/SiO$_2$ substrate monolayer structure at normal incidence of wave-length λ = 3 m, locating the cross-section at y = 0 mm. The color contour shows the amplitude of the magnetic field, while the arrows denote the instantaneous the direction of the current density. Contrast with the figs. 10(a)-10(c), the dis-

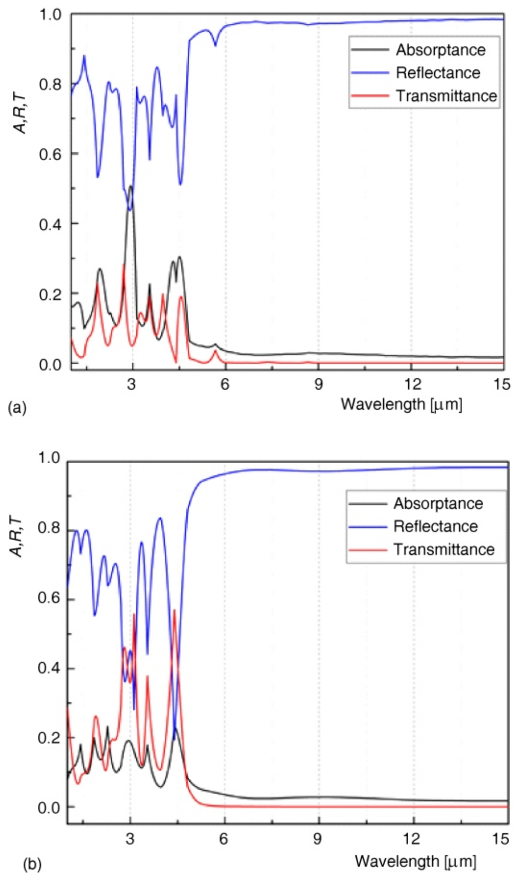

Figure 7. Absorption, transmission and reflection of Si and SiO$_2$ substrate structures; (a) Si substrate structure, (b) SiO$_2$ substrate structure

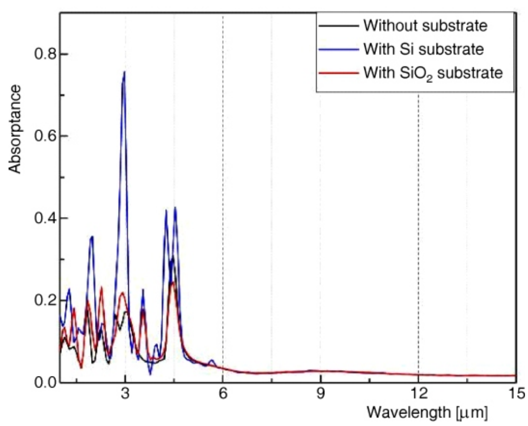

Figure 8. The absorptance of three models

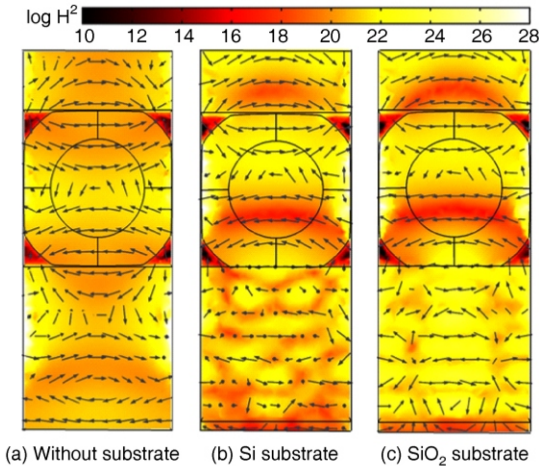

Figure 9. The current density distribution when the incidence wavelength is 3 m

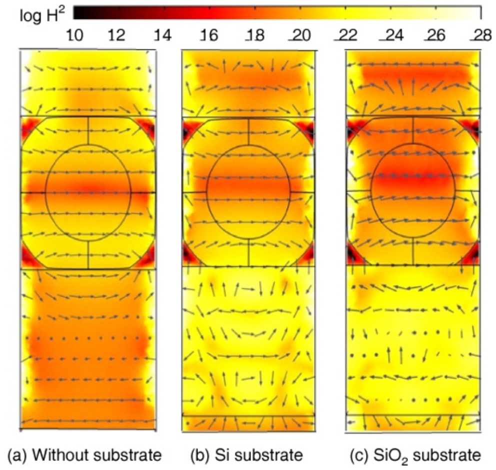

Figure 10. The current density distribution when the incidence wavelength is 4.5 μm

tribution of the electric field inside the aluminum was consistent, however, the strength of the SPR effect of the microstructure was significantly enhanced. Due to the addition of the substrate, the magnetization effect of the upper surface of the aluminum layer was enhanced, especially interior the aluminum porous monolayer, while the nether electric field was in the opposite direction, forming a completely closed loop. The formation of two groups of induction electric filds affects the initial current distribution in the porous interior. For Si and SiO_2, the relative of the material, namely *n* and *k*, caused the internal electric field deflecting directly, which formed the induction magnetic field in different directions.

Figure 10 shows the current density distribution and schematic of the aluminum porous monolayer microstructure and Si/SiO_2 substrate monolayer structure at normal incidence of wavelength $\lambda = 4.5$ m, locating the cross-section at $y = 0$ mm. At this incident frequency, contrasting fig. 9 with fig. 10, the distribution of the electric field inside the aluminum was consistent, however, the strength of the SPR effect of the microstructure enhance significantly. Due to the addition of the substrate, the magnetization effect of the upper surface of the aluminum layer enhance, especially interior the aluminum porous monolayer, while the nether electric field was in the opposite direction, forming a completely closed loop. The formation of two groups of induction electric fields affects the initial current distribution in the porous interior. It was obvious that the two closed loops formed by the induced current near the upper and lower surfaces of porous structure enhance significantly. Meanwhile, these small new magnetic loops formed within the base of the substrate further strengthen the surface plasmas of the porous structure.

Conclusions

In this paper, the spectral characteristics of the spherical porous aluminum monolayer structure in the infrared band with wavelength ranging from 1-15 m was calculated by FDTD. The distributions of the electric field and magnetic intensity were analyzed. Then the absorptive capacity of Si and SiO_2 substrate structures was considered, respectively. We have consulted the following conclusions.

The absorptive capacity of the porous structure of Si and SiO_2 substrate was calculated. It was found that in wavelength of 1~6 m, the single layer of aluminum cell structure with Si substrate could produce higher absorption peak, while the SiO_2 based structure could not at the wavelength from 6 to 15 m.

The absorptive capacity of these two structures and monolayer spherical porous aluminum cell structure had no difference.

The highest absorptance of silicon substrate was 0.76, which was three times higher than that of the porous aluminum plate.

Acknowledgment

This work is supported by the National Natural Science Foundation of China (Grant No. 51536001, No. 51776050).

Nomenclature

A – absorptance, [–]
$\boldsymbol{B}$ – magnetic flux density, [Wbm^{-2}]
$\boldsymbol{D}$ – electric displacement
$\boldsymbol{E}$ – electric field intensity, [Am^{-1}]
$\boldsymbol{H}$ – magnetic field intensity, [Vm^{-1}]
$\boldsymbol{J}$ – the current density, [Am^{-2}]
n – the unit outward normal, [–]
$Q^{(a)}$ – the absorption cross-section, [m^2]
R – reflectance, [–]
S – poynting vector, [Wm^{-2}]
T – transmittance, [–]
t – time, [s]
$W^{(a)}$ – the rate of absorption, [Ws^{-1}]
x, y, z – the axis in Cartesian co-ordinate, [–]

Greek symbols

ε – the permittivity, [Fm^{-1}]
μ – the permeability, [Sm^{-1}]
ρ – volume charge density, [Cm^{-3}]

Superscript

a – absorption
s – scattering

References

[1] Scholes, G. D., *et al*., Lessons from Nature about Solar Light Harvesting, *Nature Chemistry, 3* (2011), 10 pp. 763-774
[2] Huang, Z., *et al*., Nanoparticle Embedded Double-Layer Coating for Daytime Radiative Cooling, *International Journal of Heat and Mass Transfer, 104* (2017), Jan., pp. 890-896
[3] Wang, S., *et al*., CFD Studies of Dual Circulating Fluidized Bed Reactors for Chemical Looping Combustion Processes, *Chemical Engineering Journal, 236* (2014), Jan., pp. 121-130
[4] Bolger, P., *et al*., Amplified Spontaneous Emission of Surface Plasmon Polaritons and Limitations on the Increase of Their Propagation Length, *Optics Letters, 35* (2010), 8, pp. 1197-1199
[5] Nakkach, M., *et al*., Angulo-Spectral Surface Plasmon Resonance Imaging of Nanofabricated Grating Surfaces, *Optics Letters, 35* (2010), 13, pp. 2209-2211
[6] Jha, R., *et al*., High-Performance Sensor Based on Surface Plasmon Resonance with Chalcogenide Prism and Aluminum for Detection in Infrared, *Optics Letters, 34* (2009), 6, pp. 749-751
[7] Huang, J. G., *et al*., Narrow-Band Spectral Features of Structured Silver Surface with Rectangular Resonant Cavities, *Journal of Quantitative Spectroscopy and Radiative Transfer, 112* (2011), 5, pp. 839-846
[8] Fu, C. J., *et al*., Semiconductor thin Films Combined with Metallic Grating for Selective Improvement of Thermal Radiative Absorption/Emission, *Journal of Heat Transfer, 131* (2009), 3, 033105
[9] Chen, Y. Y., *et al*., Unusual Photon Tunneling in the Frustrated Total Internal Reflection Structure Including Indefinite Metamaterials, *Journal of Optics, 12* (2010), 4, pp. 292-295
[10] Zhang, Z. M., *et al*., Unusual Photon Tunneling in the Presence of a Layer with a Negative Refractive Index, *Applied Physics Letters, 80* (2002), 6, pp. 1097-1099
[11] Tien, C. L., Thermal Radiation Properties of Gases, *Advances in Heat Transfer, 5* (1969), Dec., pp. 253-324
[12] Mulet, J. P., *et al*., Enhanced Radiative Heat Transfer at Nanometric Distances, *Microscale Thermophysical Engineering, 6* (2002), 3, pp. 209-222
[13] Francoeur, M., *et al*., Role of Fluctuational Electrodynamics in Near-Field Radiative Heat Transfer, *Journal of Quantitative Spectroscopy and Radiative Transfer, 109* (2008), 2, pp. 280-293

[14] Liu, B., *et al.*, Near-Field Radiative Heat Transfer for Si Based Meta-Materials, *Optics Communications, 314* (2014), 3, pp. 57-65
[15] Che, Z. Z., A Fluctuational Electrodynamic Analysis of Micro/Nano Scale Radiative Transfer of Surfaces. Ph. D. thesis, Harbin Institute of Technology, Harbin, China, 2007
[16] Xuan, Y. M., *et al*., Spectrum Control Technique Based on the Surface Microstructure, *Infrared Laser Engineering, 38* (2009), 1, pp. 36-40
[17] Fu, K., *et al*., Modeling the Radiative Properties of Microscale Random Roughness Surfaces, *Journal of Heat Transfer, 129* (2007), 1, pp. 71-78
[18] Chen, Y. B., *et al*., Impacts of Geometric Modifications on Infrared Optical Responses of Metallic Slit Arrays, *Optics Express, 17* (2009), 12, pp. 9789-9803
[19] Klimov, V. V., *et al*., Radiative Decay of a Quantum Emitter Placed Near a Metal-Dielectric Lamellar Nanostructure: Fundamental Constraints, *Physical Review A, 93* (2016), 3, 033831
[20] Zheng, Y., Thermal Radiative Wavelength Selectivity of Nanostructured Layered Media, in: *Nanoscaled Films and Layers* (Ed. L. Nanai) InTech, Rijeka, Croatia, 2017
[21] Zhang, Z. M., *Nano/Microscale Heat Transfer*, Mc Graw-Hill Press, New York, USA, 2007
[22] Palik, E. D., Handbook of Optical Constants of Solids, Academic Press, New York, USA, 1998, pp. 350-357

Paper submitted: November 25, 2107
Paper revised: December 20, 2017
Paper accepted: December 21, 2017